Monolayer-like Exciton Recombination Dynamics of Multilayer $MoSe_2$ Observed by Pump-Probe Microscopy

Cullen P. Walsh, Jason P. Malizia, Sarah C. Sutton, John M. Papanikolas,* and James F. Cahoon*

Department of Chemistry, University of North Carolina at Chapel Hill, Chapel Hill, North Carolina 27599-3290, United States.

*e-mail: john_papanikolas@unc.edu; jfcahoon@unc.edu

KEYWORDS: *Pump-probe microscopy, $MoSe_2$, transition metal dichalcogenide, multilayer, recombination, excitons.*

ABSTRACT: Transition metal dichalcogenides (TMDCs) have garnered considerable interest over the past decade as a class of semiconducting layered materials. Most studies on the carrier dynamics in these materials have focused on the monolayer due to its direct bandgap, strong photoluminescence, and strongly bound excitons. However, a comparative understanding of the carrier dynamics in multilayer (e.g. >10 layers) flakes is still absent. Recent computational studies have suggested that excitons in bulk TMDCs are confined to individual layers, leading to room-temperature stable exciton populations. Using this new context, we explore the carrier dynamics in $MoSe_2$ flakes between ~16-125 layers thick. We assign kinetics to exciton-exciton annihilation (EEA) and Shockley-Read-Hall recombination of free carriers. Interestingly, the average observed EEA rate constant (0.003 cm^2/s) is nearly independent of flake thickness and two-orders of magnitude smaller than an unencapsulated monolayer (0.33 cm^2/s) but very similar to values observed in encapsulated monolayers. Thus, we posit that strong intra-layer interactions minimize

the effect of layer thickness on recombination dynamics, causing the multilayer to behave similar to the monolayer and exhibit an apparent EEA rate intrinsic to $MoSe_2$.

Transition metal dichalcogenides (TMDCs) have garnered considerable interest as a class of layered materials with semiconducting bandgaps in the visible to near-IR.[1] Their weak interlayer van der Waals interactions allow for layer-by-layer mechanical exfoliation down to the monolayer,[2] making them useful in flexible and wearable electronics.[3, 4] These materials have been extensively studied in the monolayer, which contains strongly bound excitons (coulombically bound electron-hole pairs) that dictate the optical properties.[5-10] This results in recombination dynamics dominated by exciton-exciton annihilation (EEA), an Auger recombination process, at high carrier densities.[11, 12]

In contrast, excitons in multilayer and bulk TMDCs are often considered unstable at room temperature due to early estimations of the bulk exciton binding energy at ~25 meV,[13] which is similar to values for other bulk semiconductors such as silicon and GaAs at ~14 and ~4 meV, respectively.[14] Thus, excitons are often discounted when assigning the recombination dynamics in multilayer TMDCs.[15, 16] However, recent experimental and computational studies have suggested that the exciton binding energies in bulk TMDCs are in the range of 50-150 meV, indicating that the exciton population is stable at room temperature and could contribute to the dynamics.[17-23] This is supported by experimental evidence that suggests above bandgap excitation leads to a mixture of excitons and free carriers in multilayer flakes,[24] despite some dissociation of excitons into free carriers.[25]

The unusually large exciton binding energy in bulk $MoSe_2$ is a result of spatial confinement of the exciton wavefunction to individual layers due to the predominantly planar $d_{x^2-y^2}$, d_{xy} and

$p_{x/y}$ orbital character of the excitons at the direct bandgap.[19, 20, 23, 26-31] This results in excitons that are quasi-two dimensional, similar to the excitons in the monolayer. As a result, these materials may act more like a stack of lightly interacting monolayers than a 3D bulk crystal. For instance, the exciton diffusion rate has been shown to be ~19x faster within each layer (intralayer diffusion) than across layers (interlayer diffusion).[32] Taken together, the recent reports of bound excitons and monolayer-like behavior provide a fresh motivation to analyze the recombination dynamics of multilayer TMDCs.

In this Letter, we focus on the recombination dynamics of the TMDC $MoSe_2$ by studying nanoflakes between 16±1 and 125±1 layers (10.1±0.4 and 82±1 nm) thick using a home-built optical pump-probe microscope (note that errors in flake layer numbers as determined by atomic force microscopy (AFM) imaging are ±1 layer unless noted otherwise). Ultrafast pump-probe microscopy experiments were performed as described previously (see Supporting Text).[33, 34] Typical pump powers (I_P) and probe powers (I_T) ranged from 0.75-5.00 pJ/pulse and 1.00-2.00 pJ/pulse, respectively. Photoexcitation of electrons from the valence band into the conduction band by the pump pulse causes changes in the complex refractive index of the material, which we detect via changes in the transmission of the probe beam (ΔI_T) by collecting the difference in the probe signal with and without the pump using lock-in detection. For measurements of the carrier lifetimes, the probe wavelength (λ_{probe}) was kept constant while the time delay between the pump and probe was changed to monitor ΔI_T with time. Kinetic data is normalized to I_T, and when noted I_P as well, to yield plots $\Delta I_T/I_T$ or $\Delta I_T/I_T/I_P$ for kinetic analysis (e.g. Figure S1). Measured dynamics are then correlated with changes in the exciton and free carrier populations by fitting the data via a kinetic model.

We prepared multilayer (~16-125-layers) $MoSe_2$ flakes via mechanical exfoliation onto glass substrates. The thickness of individual flakes was verified by AFM imaging (Figure S2). We optically imaged the flakes by raster scanning our probe laser spot across the sample and collecting the transmitted light, as shown in **Figure 1a** for a ~21-layer flake. We isolate the dynamics to the most uniform, central region of each flake to avoid structural features that have been shown to cause changes in the exciton binding energy[35] and free carrier population,[36] which would complicate a kinetic analysis. The relative size of our laser spot in comparison to a typical flake is illustrated in **Figure 1a**.

We measured the ground state transmission contrast (T_C) spectrum at the center of each flake by taking the difference in transmitted light on the flake versus off the flake with the background signal removed for clarity (Figure S3). An exemplary T_C spectrum for a ~21-layer flake is shown in **Figure 1b**. The spectrum shows two features at 810 and 700 nm that are attributable to absorption and reflection by A- and B-excitons in the material, respectively.[37] These excitons arise from transitions between the spin-orbit split valence and conduction bands at the K-point (**Figure 1c**).[13] In the experiments described herein, a 780 nm pump beam excites charge carriers (electrons and holes) at the blue edge of the A-exciton transition (**Figure 1b**), resulting in an initial population of primarily A-excitons and a negligible population of B-excitons. We determined that data collected with probe wavelengths to the red of the exciton transition (λ_{probe} > 860 nm) primarily reflect changes in the excited net carrier population of excitons and free carriers (Figure S4).

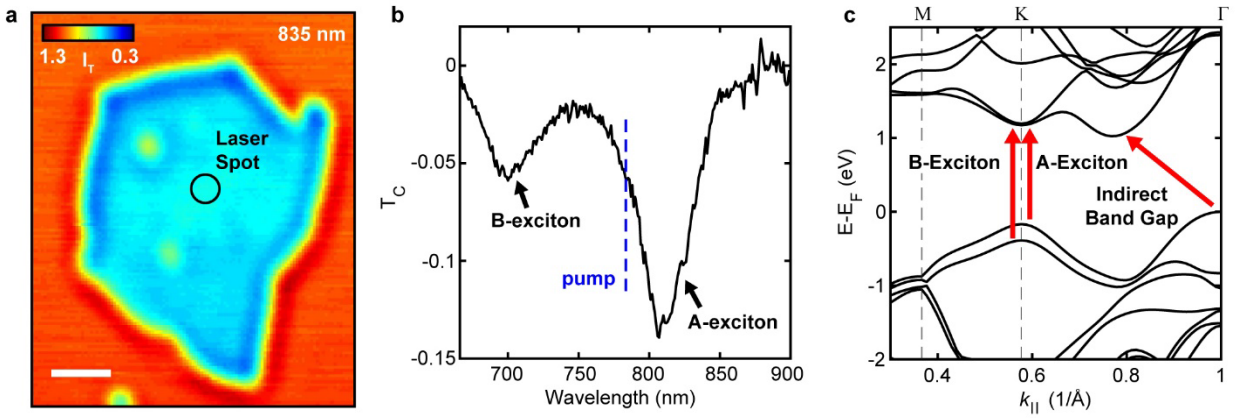

Figure 1. Multilayer $MoSe_2$ ground state. (**a**) Probe-only transmission image at λ_{probe} = 835 nm for a ~21-layer $MoSe_2$ flake with the laser spot size shown for comparison; scale bar, 2 μm. (**b**) T_C spectrum from the center of the ~21-layer flake showing the A- and B-exciton transitions in the material. (**c**) Band diagram of bulk $MoSe_2$ showing the indirect transition and the A- and B-exciton transitions at the K-point.

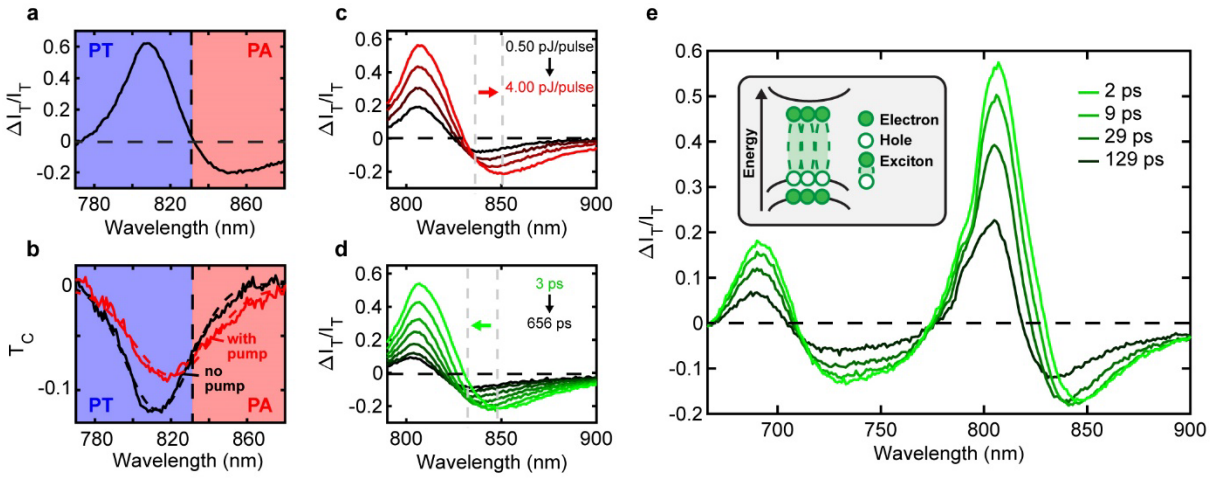

Figure 2. Spectral signatures of the exciton recombination dynamics. (**a-b**) Transient pump-probe spectrum (panel a) and T_C spectra (panel b) with the pump blocked (black curves) and the pump present (red curves) for a ~21-layer flake with I_P = 5.00 pJ/pulse and 1 ps delay. The areas

of PT and PA are shaded blue and red, respectively. Dashed lines in panel b represent fits to Gaussian functions. (**c**) Transient spectra taken at 1 ps with increasing I_P (0.50, 1.00, 2.00, 4.00 pJ/pulse). (**d**) Transient spectra taken at I_P = 5.00 pJ/pulse with increasing time delay (3, 17, 43, 90, 190, 390 and 656 ps). (**e**) Transient spectra taken at I_P = 4.00 pJ/pulse comparing the A- and B-exciton transitions for a ~21-layer flake at multiple time delays. Inset: Illustration of the energy bands and the photoexcited A-exciton population.

To begin investigating the exciton dynamics in the multilayer, we collected transient spectra that span the A-exciton resonance (770-880 nm). In **Figure 2a** we show a representative transient spectrum collected from a ~21-layer flake at 1 ps with I_P = 5.00 pJ/pulse. The spectrum exhibits a positive peak around the exciton resonance and a negative peak to the red of the exciton resonance. To understand the origin of these features, we compare the shape of T_C spectra for the A-exciton transition with and without the pump in **Figure 2b**. We fit the A-exciton peaks via Gaussians and find that in the presence of the pump, the exciton resonance redshifts and widens while the area decreases. This redshift and widening of the exciton resonance leads to areas of photo-induced absorption (PA) with negative $\Delta I_T/I_T$ signal (red regions) and areas of photo-induced transparency (PT) with positive $\Delta I_T/I_T$ signal (blue regions). We observed the same result across all the flakes we studied, although the relative amplitude of the PA changes non-linearly with thickness due to coherent etalon-type reflections that change the shape of the ground state exciton transition (Figure S5).[38] The origin of these spectral features are discussed in the Supporting Text.

Transient spectra collected at increasing I_P (0.50-4.00 pJ/pulse) at 1 ps show the PA peak increasingly redshifts with increasing I_P (**Figure 2c**), while transient spectra collected at I_P = 5.00

pJ/pulse and multiple time delays show the PA peak shifts back towards the blue with increasing time delay (**Figure 2d**). These trends are attributable to an interplay between the widening and shifting of the exciton resonance that is difficult to disentangle simply by fitting the transient spectra.[39] We also collected transient spectra across both the A- and B-exciton resonances (666-900 nm). In **Figure 2e**, we show a representative transient spectrum collected from a ~21-layer flake at I_P = 4.00 pJ/pulse, with similar results observed for other flakes. The spectrum shows that unlike the A-exciton resonance, the B-exciton resonance does not exhibit a blueshift in the PA feature at increasing time delays. In these experiments, we are directly photoexciting the A-exciton resonance and thus expect an initially high A-exciton population and negligible B-exciton population. We therefore posit that the spectral shifts of the A-exciton PA peak are primarily caused by interactions involving the large A-exciton population that are net stabilizing. These interactions can also lead to a further widening of the peak due to exciton-exciton scattering. At the same time, there are still PA and PT peaks at the B-exciton transition, indicating that the B-exciton transition is being perturbed even without a substantive B-exciton population. We attribute this to a change in the background potential induced by the photoexcited A-excitons and free carriers.[5] This will result in both exciton screening and bandgap renormalization, causing a small redshift of the B-exciton transition.

Next, the recombination dynamics were analyzed to determine contributions from both excitons and free carriers. A representative kinetic trace and transient images from the center of a ~21-layer flake collected at λ_{probe} = 870 nm are shown in **Figure 3a**. At 0 ps, the pump and probe are temporally overlapped and the pump-excited carrier population causes a negative spike in the transient signal. As the time delay increases, the photoexcited carriers recombine, which causes the signal to exponentially decay. As apparent from the pump-probe images in **Figure 3a** at several

select time delays, the rate of decay is consistent across multiple locations on the flake, excluding edges and structural features, and this consistency was true for every flake studied.

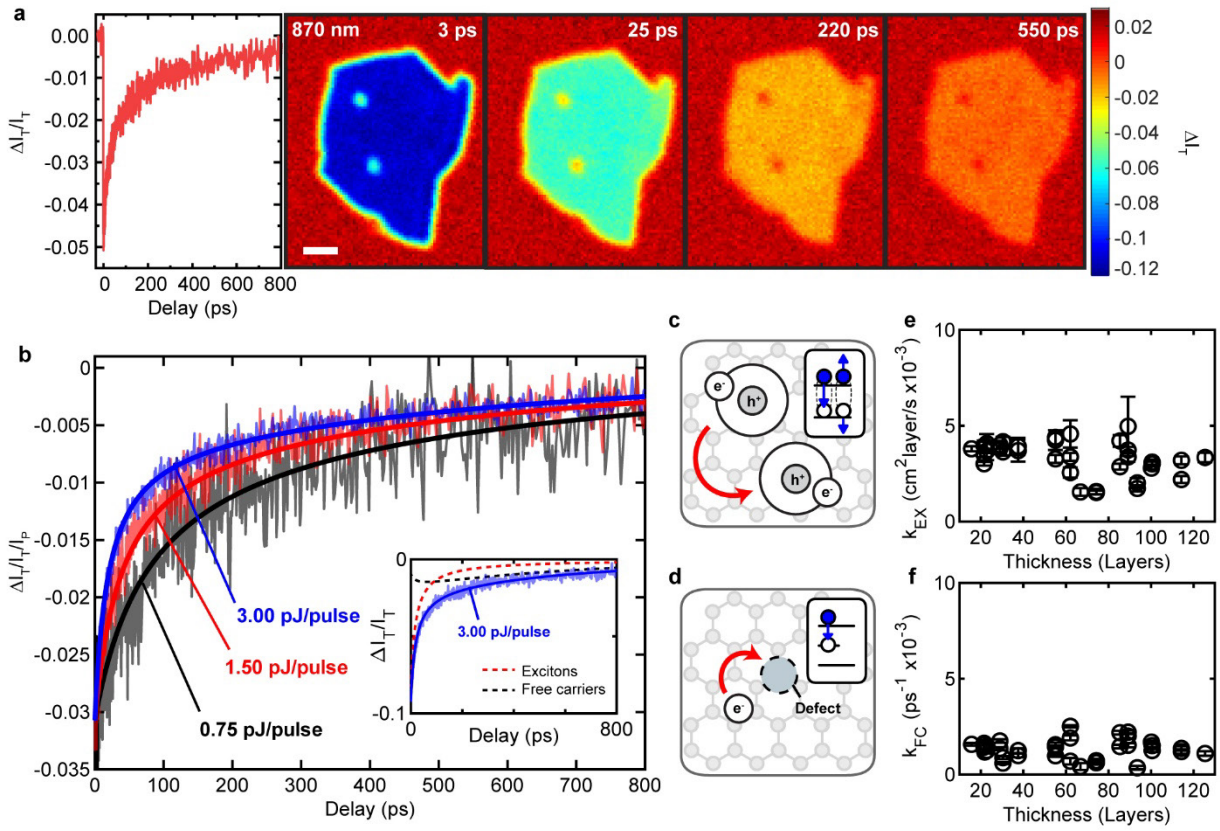

Figure 3. Recombination kinetics. (**a**) Left: kinetics taken from the center of a ~21-layer flake at λ_{probe} = 870 nm and I_P = 1.50 pJ/pulse. Right: images taken of the same flake at λ_{probe} = 870 nm and I_P = 5.00 pJ/pulse at multiple time delays; scale bar, 2 μm. (**b**) Kinetic traces at λ_{probe} = 870 nm normalized to pump powers of I_P = 0.75 (black), 1.50 (red), and 3.00 (blue) pJ/pulse for a 21±1-layer flake. Solid lines represent fits to the data. Inset: free carrier (black dashed line) and exciton (red dashed line) contributions to the total kinetic fit (blue solid line) for the I_P = 3.00 pJ/pulse data. (**c**-**d**) Illustrations of EEA (panel c) and SRH recombination (panel d). (**e**) EEA rate constant with increasing flake thicknesses. (**f**) SRH recombination rate constant with

increasing flake thicknesses. Vertical error bars indicate the 95% confidence interval for each rate constant while horizontal error bars range from 0.3 to 2.6 layers and are omitted for clarity.

To investigate the presence of non-linear recombination processes, we collected kinetic traces at increasing I_P (0.75-3.00 pJ/pulse). The transient signal at 0 ps increases linearly with I_P, which suggests that our signal intensity can be linearly correlated to the density of photoexcited carriers and that non-linear processes, such as saturable absorption[12] and two-photon absorption[40], are negligible (Figure S6). With the traces normalized via I_P (**Figure 3b**), the data show that the signal decays faster as I_P increases. This indicates that the rate of decay scales with the net carrier population and that many-body recombination processes are occurring. We performed the same experiment across flakes of increasing thickness and observed the same trend.

To compare the recombination rate at each thickness, all kinetic traces were fit using a kinetic model for the decay of the net charge carrier density, ρ. In our experiments, we expect that the initial ρ at 0 ps consists of both a population of excitons, $\rho_{EX,}$ and of free carriers, $\rho_{FC.}$ Based on our kinetic analysis and fitting using eq. S11 (see Supporting Text), we assign the recombination of the exciton population to EEA (k_{EX}), which is a second-order Auger process[41] that results from the collision of two excitons where one exciton recombines and the other exciton is ionized, forming an electron and/or hole with excess energy relative to the bandgap (**Figure 3c**).[11, 12] We assign recombination of the free carrier population to Shockley-Read-Hall (SRH) recombination (k_{FC}), which is a pseudo first-order process in which free carriers recombine via material defects (**Figure 3d**).[42]

We determined k_{EX} and k_{FC} as a function of thickness (**Figure 3e,f**) by performing global fits of the kinetic traces at I_P values ranging from 0.75-4.00 pJ/pulse for 16 flakes of thicknesses

varying from ~16-125 layers. An exemplary fit for a ~21-layer flake is shown in **Figure 3b** along with the individual contributions at I_P = 3.00 pJ/pulse (inset of **Figure 3b**) from the excitons and free carriers. The fit shows that at the highest I_P, EEA dominates the kinetics within the first ~100 ps. Then, once most excitons have recombined, the signal is dominated by the slower decay of the free carriers, which occurs over hundreds of picoseconds.

We found that k_{FC} is relatively constant with increasing flake thickness, resulting in an average SRH recombination rate constant of k_{FC} = 0.0013±0.0005 ps^{-1}. To compare k_{EX} across flakes of different thicknesses, we calculated the rate in terms of the areal number density per layer (#/cm^2/layer) or equivalently (within a constant equal to the thickness per layer) the volumetric number density (#/cm^3). When calculating k_{EX}, we converted from pump power to photoexcited carrier concentration using a beam radius of 400 nm and assuming an initial ratio of $\rho_{FC,o}/\rho_{EX,o}$ = 1. We also calculated the net absorption at each flake thickness using a dielectric model based on the Lorentz dipole oscillator model (see Supporting Text). These absorption values account for resonant enhancements and reductions in the amount of absorbed light at varying thicknesses caused by coherent reflections in the material (Figure S8).[38] Across all thicknesses, we extract an average EEA rate constant of k_{EX} = (3.3±0.9)x10^{-3} cm^2layer/s.

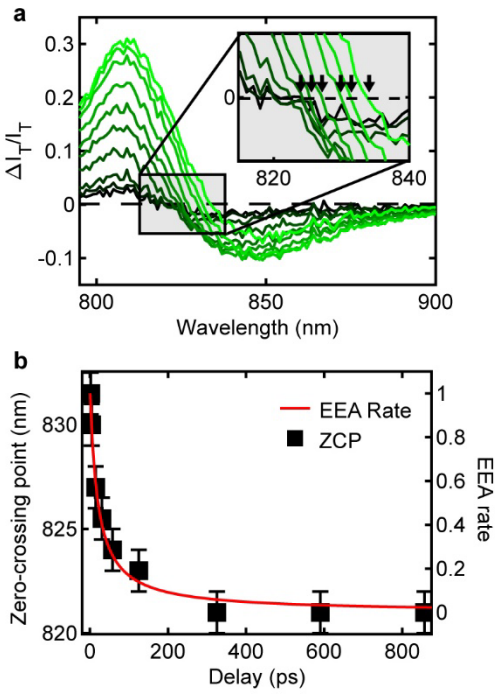

Figure 4. Spectral shifts and kinetics caused by EEA. (**a**) Transient spectra collected at $I_P = 3.00$ pJ/pulse showing the change in the zero-crossing point in time. (**b**) Comparison of the transient spectra zero-crossing point at increasing time delays and the normalized EEA rate for the same flake.

To verify this kinetic analysis, we compared the fits to the spectral shifts observed for the A-exciton peak. In Figure 2e, we posited that the spectral shifts of the A-exciton peak are primarily caused by interactions involving the large A-exciton population that are net stabilizing. These spectral shifts should therefore decay away as the A-exciton population recombines through EEA. We quantified the kinetics of the spectral shift using the zero-crossing point (ZCP), the wavelength in the transient spectrum at which the signal crosses from positive to negative. This point is affected by both the PT and PA peaks and therefore serves as a proxy for the net perturbations of the exciton resonance. Using transient spectra (**Figure 4a**) collected at $I_P = 3.00$ pJ/pulse, we plot

the wavelength of the ZCPs at various time delays in **Figure 4b**. The ZCPs are then compared to the fit of the normalized second-order EEA kinetics extracted for the same flake. We observe a strong overlap between the rate of the second-order EEA kinetics and the change in the ZCP in time. Thus, the second-order kinetics of the exciton ZCP feature strongly indicates that the observed dynamics result from exciton-exciton interactions consistent with recombination of the exciton population through EEA. It also reaffirms that the changes in the exciton resonance, including the exciton linewidth and energy, are primarily caused by the A-exciton population, not the free carriers.

Remarkably, the EEA rate constant, k_{EX}, that we measured is ~2 orders of magnitude smaller than the previously reported monolayer EEA rate of 0.33 cm^2/s.[12] To rationalize this precipitous drop in the EEA rate going from the monolayer to the multilayer, we first consider the two components of EEA[43]: the exciton collision frequency, v, and the recombination probability per collision, B, where

$$k_{EX} \propto Bv. \quad (1)$$

The exciton collision frequency, v, depends on both the exciton diameter and the average exciton velocity. In $MoSe_2$, excitons become more spatially diffuse going from the monolayer to the multilayer due to a decrease in the exciton binding energy from ~650[44] to ~150 meV.[20] There is also an increase in the exciton diffusion rate going from the monolayer (12 cm^2/s) to the bulk (19 cm^2/s).[32] Given these changes, we would intuitively expect a higher exciton collision frequency, and hence a faster k_{EX}, in the multilayer. However, this is not what we observe. Instead, we attribute the drop in k_{EX} going from the monolayer to the multilayer to surface effects.

In $MoSe_2$, the excitons in the exterior and interior layers experience different environments, with the exterior layers in contact with the substrate and air and the interior layers encapsulated by

neighboring $MoSe_2$ layers. This should result in different exciton recombination rates for the interior and exterior layers. For instance, at the $MoSe_2/SiO_2$ interface, excitons can become localized due to potential fluctuations caused by the roughness of the substrate, bubbles formed by surface contamination, and fixed charges near the surface (**Figure 5**).[45-47] These features can cause lattice strain and changes in the dielectric environment, resulting in a spatially inhomogeneous bandgap with potential energy minima where excitons will collect. These localized exciton densities will then have a higher collision frequency, v, leading to a faster EEA rate. Similar potential fluctuations can occur for the surface layer due to adsorbates (**Figure 5**). At the same time, charged defects at the $MoSe_2/SiO_2$ interface can trap excitons, leading to long-lived, immobile trap states that can act as efficient nonradiative recombination centers for freely diffusing excitons.[48] In contrast, the interior layers should be relatively insulated from these potential fluctuations and charged defects.

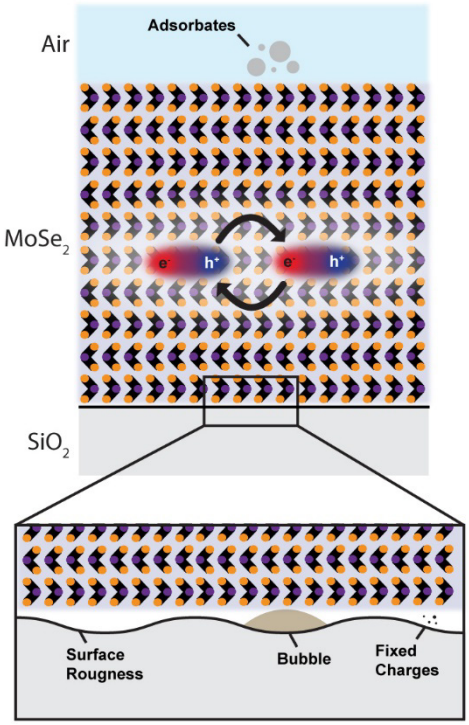

Figure 5. Surface versus bulk recombination within multilayer $MoSe_2$. Upper: illustration of 10-layer $MoSe_2$ showing a top air interface with adsorbates and bottom interface with the substrate. Recombination of excitons primarily confined within one 2D layer is also illustrated. Lower: detail of the $MoSe_2$/substrate interface showing surface roughness, bubbles, and fixed charges that tend to induce charge carrier recombination.

These surface effects will result in exterior layers that induce a faster EEA rate than the interior layers. However, if excitations are primarily confined to individual layers, then multilayer flakes of sufficient thickness would be expected to have recombination dynamics that are independent of thickness and relatively unaffected by surface defects. But if excitations can quickly diffuse throughout the 3D bulk of the flake, then as the ratio of interior-to-exterior layers increases, the effective EEA rate constant would be increasingly less affected by the surface and become progressively lower, scaling as the inverse of thickness. Such behavior has previously been observed in nanoscale systems such as silicon nanowires,[49] where the recombination rate constant scales with the inverse of diameter. Here, the independence of k_{EX} with layer thickness thus strongly supports confinement of excitations to individual layers, consistent with a high intra-layer exciton confinement and slow out-of-plane diffusion.

Similar low values of k_{EX} have been observed from encapsulated monolayers where the TMDC is surrounded on top and bottom by layers of atomically flat hexagonal boron nitride, preventing surface roughness and charged impurities.[45, 50] Upon encapsulation, k_{EX} in the monolayer has been shown to drop by two orders of magnitude, from 0.12 in the unencapsulated form to 0.0063 cm^2/s in the encapsulated form for monolayer WS_2.[45] This encapsulated k_{EX} can be interpreted as the intrinsic recombination rate constant for the TMDC, independent of surface

effects and the external environment. The equivalently low k_{EX} that we observe for the multilayer suggests that the EEA rate in the multilayer is likewise the intrinsic recombination rate for $MoSe_2$, further indicating that multilayer $MoSe_2$ acts as a stack of individual monolayers encapsulated by neighboring $MoSe_2$ layers rather than as a typical bulk crystal.

In summary, we studied the recombination dynamics of multilayer $MoSe_2$ and determined that the dynamics are dominated by EEA at early time delays, followed by a slow defect-mediated decay of the free carrier population. We found that the EEA rate constant was independent of flake thickness and that the average EEA rate constant (0.003 cm^2layer/s) that we extracted for flakes between ~16-125 layers is around two-orders of magnitude slower than what has been reported for the unencapsulated monolayer (0.33 cm^2/s).[12] This is consistent with multilayer stacks in which recombination is minimally affected by surfaces and instead dominated by intra-layer interactions of charge carriers primarily confined within one layer. Based on a comparison to the encapsulated monolayer, we posit that the EEA rate in the multilayer is the intrinsic recombination rate of $MoSe_2$. Overall, the results suggest that the multilayer acts as a stack of lightly interacting, encapsulated monolayers as opposed to a typical bulk crystal. This will have important implications for the incorporation of multilayer TMDCs into future optoelectronic devices.

Supporting Information

Additional details on the experimental setup, description of the origin of the spectral features, kinetic fitting equations, description of dielectric model for simulating absorption values and spectral features, plots of the constituent parts of the transient spectra, atomic force microscopy images, plots of the transmission contrast spectra with and without baseline removal, comparison

of transient spectra at varying I_P and varying time delays, dielectric model simulations of transient spectra and transmission contrast spectra at multiple flake thicknesses, $\Delta I_T/I_T$ at 0 ps time delay and increasing I_P, comparison of fitting coefficients for the kinetic traces, dielectric model simulations of the absorption values at increasing flake thicknesses, and average rate constants at each flake thickness.

Author Information

Corresponding Authors

*E-mail: john_papanikolas@unc.edu; jfcahoon@unc.edu

Acknowledgements

This work was supported by a grant from the National Science Foundation (DMR-1764228). C.P.W. acknowledges partial support from the NC Space Grant, and S.C.S acknowledges an individual NSF graduate research fellowship. Atomic force microscopy imaging was performed at the Chapel Hill Analytical and Nanofabrication Laboratory (CHANL), a member of the North Carolina Research Triangle Nanotechnology Network (RTNN), which is supported by the NSF (ECCS-2025064) as part of the National Nanotechnology Coordinated Infrastructure.

Abbreviations

TMDC, transition metal dichalcogenide, T_C, transmission contrast, ps, picosecond, PA, photo-induced absorption, PT, photo-induced transparency, SRH, Shockley-Read-Hall, ZCP, zero crossing point.

References

1. Butler, S. Z.; Hollen, S. M.; Cao, L.; Cui, Y.; Gupta, J. A.; Gutiérrez, H. R.; Heinz, T. F.; Hong, S. S.; Huang, J.; Ismach, A. F.; Johnston-Halperin, E.; Kuno, M.; Plashnitsa, V. V.;

Robinson, R. D.; Ruoff, R. S.; Salahuddin, S.; Shan, J.; Shi, L.; Spencer, M. G.; Terrones, M.; Windl, W.; Goldberger, J. E. Progress, Challenges, and Opportunities in Two-Dimensional Materials Beyond Graphene. *ACS Nano* **2013,** *7*, (4), 2898-2926.

2. Novoselov, K. S.; Jiang, D.; Schedin, F.; Booth, T. J.; Khotkevich, V. V.; Morozov, S. V.; Geim, A. K. Two-dimensional atomic crystals. *Proc. Natl. Acad. Sci.* **2005,** *102*, (30), 10451-10453.
3. Singh, E.; Singh, P.; Kim, K. S.; Yeom, G. Y.; Nalwa, H. S. Flexible Molybdenum Disulfide (MoS_2) Atomic Layers for Wearable Electronics and Optoelectronics. *ACS Appl. Mater. Interfaces* **2019,** *11*, (12), 11061-11105.
4. Yao, J.; Yang, G. 2D group 6 transition metal dichalcogenides toward wearable electronics and optoelectronics. *J. Appl. Phys.* **2020,** *127*, (3), 030902.
5. Pogna, E. A. A.; Marsili, M.; De Fazio, D.; Dal Conte, S.; Manzoni, C.; Sangalli, D.; Yoon, D.; Lombardo, A.; Ferrari, A. C.; Marini, A.; Cerullo, G.; Prezzi, D. Photo-Induced Bandgap Renormalization Governs the Ultrafast Response of Single-Layer MoS_2. *ACS Nano* **2016,** *10*, (1), 1182-1188.
6. Zhao, J.; Zhao, W.; Du, W.; Su, R.; Xiong, Q. Dynamics of exciton energy renormalization in monolayer transition metal disulfides. *Nano Res.* **2020,** *13*, (5), 1399-1405.
7. Sim, S.; Park, J.; Song, J.-G.; In, C.; Lee, Y.-S.; Kim, H.; Choi, H. Exciton dynamics in atomically thin MoS_2: Interexcitonic interaction and broadening kinetics. *Phys. Rev. B* **2013,** *88*, (7), 075434.
8. Sie, E. J.; Steinhoff, A.; Gies, C.; Lui, C. H.; Ma, Q.; Rösner, M.; Schönhoff, G.; Jahnke, F.; Wehling, T. O.; Lee, Y. H.; Kong, J.; Jarillo-Herrero, P.; Gedik, N. Observation of Exciton Redshift–Blueshift Crossover in Monolayer WS_2. *Nano Lett.* **2017,** *17*, (7), 4210-4216.
9. Ruppert, C.; Chernikov, A.; Hill, H. M.; Rigosi, A. F.; Heinz, T. F. The Role of Electronic and Phononic Excitation in the Optical Response of Monolayer WS_2 after Ultrafast Excitation. *Nano Lett.* **2017,** *17*, (2), 644-651.
10. Chernikov, A.; Ruppert, C.; Hill, H. M.; Rigosi, A. F.; Heinz, T. F. Population inversion and giant bandgap renormalization in atomically thin WS_2 layers. *Nat. Photon.* **2015,** *9*, (7), 466-470.
11. Sun, D.; Rao, Y.; Reider, G. A.; Chen, G.; You, Y.; Brézin, L.; Harutyunyan, A. R.; Heinz, T. F. Observation of Rapid Exciton–Exciton Annihilation in Monolayer Molybdenum Disulfide. *Nano Lett.* **2014,** *14*, (10), 5625-5629.
12. Kumar, N.; Cui, Q.; Ceballos, F.; He, D.; Wang, Y.; Zhao, H. Exciton-exciton annihilation in $MoSe_2$ monolayers. *Phys. Rev. B* **2014,** *89*, (12), 125427.
13. Cheiwchanchamnangij, T.; Lambrecht, W. R. L. Quasiparticle band structure calculation of monolayer, bilayer, and bulk MoS_2. *Phys. Rev. B* **2012,** *85*, (20), 205302.
14. Fox, M., *Optical Properties of Solids*. OUP Oxford: 2010.
15. Kumar, N.; He, J.; He, D.; Wang, Y.; Zhao, H. Charge carrier dynamics in bulk MoS_2 crystal studied by transient absorption microscopy. *J. Appl. Phys.* **2013,** *113*, (13), 133702.
16. Völzer, T.; Lütgens, M.; Fennel, F.; Lochbrunner, S. Recombination dynamics of optically excited charge carriers in bulk MoS_2. *J. Phys. B: At., Mol. Opt. Phys.* **2017,** *50*, (19), 194003.

17. Chernikov, A.; Berkelbach, T. C.; Hill, H. M.; Rigosi, A.; Li, Y.; Aslan, O. B.; Reichman, D. R.; Hybertsen, M. S.; Heinz, T. F. Exciton Binding Energy and Nonhydrogenic Rydberg Series in Monolayer WS_2. *Phys. Rev. Lett.* **2014,** *113*, (7), 076802.
18. Komsa, H.-P.; Krasheninnikov, A. V. Effects of confinement and environment on the electronic structure and exciton binding energy of MoS_2 from first principles. *Phys. Rev. B* **2012,** *86*, (24), 241201.
19. Saigal, N.; Sugunakar, V.; Ghosh, S. Exciton binding energy in bulk MoS_2: A reassessment. *Appl. Phys. Lett.* **2016,** *108*, (13), 132105.
20. Arora, A.; Deilmann, T.; Marauhn, P.; Drüppel, M.; Schneider, R.; Molas, M. R.; Vaclavkova, D.; Michaelis de Vasconcellos, S.; Rohlfing, M.; Potemski, M.; Bratschitsch, R. Valley-contrasting optics of interlayer excitons in Mo- and W-based bulk transition metal dichalcogenides. *Nanoscale* **2018,** *10*, (33), 15571-15577.
21. Meckbach, L.; Stroucken, T.; Koch, S. W. Influence of the effective layer thickness on the ground-state and excitonic properties of transition-metal dichalcogenide systems. *Phys. Rev. B* **2018,** *97*, (3), 035425.
22. Das, S.; Gupta, G.; Majumdar, K. Layer degree of freedom for excitons in transition metal dichalcogenides. *Phys. Rev. B* **2019,** *99*, (16), 165411.
23. Jindal, V.; Bhuyan, S.; Deilmann, T.; Ghosh, S. Anomalous behavior of the excited state of the A exciton in bulk WS_2. *Phys. Rev. B* **2018,** *97*, (4), 045211.
24. Tsokkou, D.; Yu, X.; Sivula, K.; Banerji, N. The Role of Excitons and Free Charges in the Excited-State Dynamics of Solution-Processed Few-Layer MoS_2 Nanoflakes. *J. Phys. Chem. C* **2016,** *120*, (40), 23286-23292.
25. Blackburn, J. L.; Zhang, H.; Myers, A. R.; Dunklin, J. R.; Coffey, D. C.; Hirsch, R. N.; Vigil-Fowler, D.; Yun, S. J.; Cho, B. W.; Lee, Y. H.; Miller, E. M.; Rumbles, G.; Reid, O. G. Measuring Photoexcited Free Charge Carriers in Mono- to Few-Layer Transition-Metal Dichalcogenides with Steady-State Microwave Conductivity. *J. Phys. Chem. Lett.* **2020,** *11*, (1), 99-107.
26. Arora, A.; Drüppel, M.; Schmidt, R.; Deilmann, T.; Schneider, R.; Molas, M. R.; Marauhn, P.; Michaelis de Vasconcellos, S.; Potemski, M.; Rohlfing, M.; Bratschitsch, R. Interlayer excitons in a bulk van der Waals semiconductor. *Nat. Commun.* **2017,** *8*, (1), 639.
27. Molina-Sánchez, A.; Sangalli, D.; Hummer, K.; Marini, A.; Wirtz, L. Effect of spin-orbit interaction on the optical spectra of single-layer, double-layer, and bulk MoS_2. *Phys. Rev. B* **2013,** *88*, (4), 045412.
28. Klein, J.; Wierzbowski, J.; Regler, A.; Becker, J.; Heimbach, F.; Müller, K.; Kaniber, M.; Finley, J. J. Stark Effect Spectroscopy of Mono- and Few-Layer MoS_2. *Nano Lett.* **2016,** *16*, (3), 1554-1559.
29. Bertoni, R.; Nicholson, C. W.; Waldecker, L.; Hübener, H.; Monney, C.; De Giovannini, U.; Puppin, M.; Hoesch, M.; Springate, E.; Chapman, R. T.; Cacho, C.; Wolf, M.; Rubio, A.; Ernstorfer, R. Generation and Evolution of Spin-, Valley-, and Layer-Polarized Excited Carriers in Inversion-Symmetric WSe_2. *Phys. Rev. Lett.* **2016,** *117*, (27), 277201.
30. Bradley, A. J.; M. Ugeda, M.; da Jornada, F. H.; Qiu, D. Y.; Ruan, W.; Zhang, Y.; Wickenburg, S.; Riss, A.; Lu, J.; Mo, S.-K.; Hussain, Z.; Shen, Z.-X.; Louie, S. G.; Crommie,

M. F. Probing the Role of Interlayer Coupling and Coulomb Interactions on Electronic Structure in Few-Layer $MoSe_2$ Nanostructures. *Nano Lett.* **2015,** *15*, (4), 2594-2599.

31. Latini, S.; Olsen, T.; Thygesen, K. S. Excitons in van der Waals heterostructures: The important role of dielectric screening. *Phys. Rev. B* **2015,** *92*, (24), 245123.
32. Kumar, N.; Cui, Q.; Ceballos, F.; He, D.; Wang, Y.; Zhao, H. Exciton diffusion in monolayer and bulk $MoSe_2$. *Nanoscale* **2014,** *6*, (9), 4915-4919.
33. Grumstrup, E. M.; Gabriel, M. M.; Cating, E. E. M.; Van Goethem, E. M.; Papanikolas, J. M. Pump–probe microscopy: Visualization and spectroscopy of ultrafast dynamics at the nanoscale. *Chem. Phys.* **2015,** *458*, 30-40.
34. Mehl, B. P.; Kirschbrown, J. R.; Gabriel, M. M.; House, R. L.; Papanikolas, J. M. Pump–Probe Microscopy: Spatially Resolved Carrier Dynamics in ZnO Rods and the Influence of Optical Cavity Resonator Modes. *J. Phys. Chem. B.* **2013,** *117*, (16), 4390-4398.
35. Yore, A. E.; Smithe, K. K. H.; Crumrine, W.; Miller, A.; Tuck, J. A.; Redd, B.; Pop, E.; Wang, B.; Newaz, A. K. M. Visualization of Defect-Induced Excitonic Properties of the Edges and Grain Boundaries in Synthesized Monolayer Molybdenum Disulfide. *J. Phys. Chem. C* **2016,** *120*, (42), 24080-24087.
36. Gibertini, M.; Marzari, N. Emergence of One-Dimensional Wires of Free Carriers in Transition-Metal-Dichalcogenide Nanostructures. *Nano Lett.* **2015,** *15*, (9), 6229-6238.
37. Shi, H.; Yan, R.; Bertolazzi, S.; Brivio, J.; Gao, B.; Kis, A.; Jena, D.; Xing, H. G.; Huang, L. Exciton Dynamics in Suspended Monolayer and Few-Layer MoS_2 2D Crystals. *ACS Nano* **2013,** *7*, (2), 1072-1080.
38. Munkhbat, B.; Baranov, D. G.; Stührenberg, M.; Wersäll, M.; Bisht, A.; Shegai, T. Self-Hybridized Exciton-Polaritons in Multilayers of Transition Metal Dichalcogenides for Efficient Light Absorption. *ACS Photon.* **2019,** *6*, (1), 139-147.
39. Wang, R.; Ruzicka, B. A.; Kumar, N.; Bellus, M. Z.; Chiu, H.-Y.; Zhao, H. Optical pump-probe studies of carrier dynamics in few-layer MoS_2. *arXiv preprint arXiv:1110.6643* **2011**.
40. Zhang, S.; Dong, N.; McEvoy, N.; O'Brien, M.; Winters, S.; Berner, N. C.; Yim, C.; Li, Y.; Zhang, X.; Chen, Z.; Zhang, L.; Duesberg, G. S.; Wang, J. Direct Observation of Degenerate Two-Photon Absorption and Its Saturation in WS_2 and MoS_2 Monolayer and Few-Layer Films. *ACS Nano* **2015,** *9*, (7), 7142-7150.
41. Yuan, L.; Huang, L. Exciton dynamics and annihilation in WS_2 2D semiconductors. *Nanoscale* **2015,** *7*, (16), 7402-7408.
42. Chi, Z.; Chen, H.; Chen, Z.; Zhao, Q.; Chen, H.; Weng, Y.-X. Ultrafast Energy Dissipation via Coupling with Internal and External Phonons in Two-Dimensional MoS_2. *ACS Nano* **2018,** *12*, (9), 8961-8969.
43. Li, Q.; Lian, T. Area- and Thickness-Dependent Biexciton Auger Recombination in Colloidal CdSe Nanoplatelets: Breaking the "Universal Volume Scaling Law". *Nano Lett.* **2017,** *17*, (5), 3152-3158.
44. Ugeda, M. M.; Bradley, A. J.; Shi, S.-F.; da Jornada, F. H.; Zhang, Y.; Qiu, D. Y.; Ruan, W.; Mo, S.-K.; Hussain, Z.; Shen, Z.-X.; Wang, F.; Louie, S. G.; Crommie, M. F. Giant bandgap renormalization and excitonic effects in a monolayer transition metal dichalcogenide semiconductor. *Nat. Mater.* **2014,** *13*, (12), 1091-1095.

45. Hoshi, Y.; Kuroda, T.; Okada, M.; Moriya, R.; Masubuchi, S.; Watanabe, K.; Taniguchi, T.; Kitaura, R.; Machida, T. Suppression of exciton-exciton annihilation in tungsten disulfide monolayers encapsulated by hexagonal boron nitrides. *Phys. Rev. B* **2017,** *95*, (24), 241403.
46. Raja, A.; Waldecker, L.; Zipfel, J.; Cho, Y.; Brem, S.; Ziegler, J. D.; Kulig, M.; Taniguchi, T.; Watanabe, K.; Malic, E.; Heinz, T. F.; Berkelbach, T. C.; Chernikov, A. Dielectric disorder in two-dimensional materials. *Nat. Nanotechnol.* **2019,** *14*, (9), 832-837.
47. Rosenberger, M. R.; Chuang, H.-J.; McCreary, K. M.; Hanbicki, A. T.; Sivaram, S. V.; Jonker, B. T. Nano-"Squeegee" for the Creation of Clean 2D Material Interfaces. *ACS Appl. Mater. Interfaces* **2018,** *10*, (12), 10379-10387.
48. Goodman, A. J.; Lien, D. H.; Ahn, G. H.; Spiegel, L. L.; Amani, M.; Willard, A. P.; Javey, A.; Tisdale, W. A. Substrate-Dependent Exciton Diffusion and Annihilation in Chemically Treated MoS_2 and WS_2. *J. Phys. Chem. C* **2020,** *124*, (22), 12175-12184.
49. Grumstrup, E. M.; Gabriel, M. M.; Cating, E. M.; Pinion, C. W.; Christesen, J. D.; Kirschbrown, J. R.; Vallorz, E. L., III; Cahoon, J. F.; Papanikolas, J. M. Ultrafast Carrier Dynamics in Individual Silicon Nanowires: Characterization of Diameter-Dependent Carrier Lifetime and Surface Recombination with Pump–Probe Microscopy. *J. Phys. Chem. C* **2014,** *118*, (16), 8634-8640.
50. Zipfel, J.; Kulig, M.; Perea-Causín, R.; Brem, S.; Ziegler, J. D.; Rosati, R.; Taniguchi, T.; Watanabe, K.; Glazov, M. M.; Malic, E.; Chernikov, A. Exciton diffusion in monolayer semiconductors with suppressed disorder. *Phys. Rev. B* **2020,** *101*, (11), 115430.

Table of contents